Journal of Non-Newtonian Fluid Mechanics 258 (2018) 45–57

Contents lists available at ScienceDirect

Journal of Non-Newtonian Fluid Mechanics

journal homepage: www.elsevier.com/locate/jnnfm

Axisymmetric viscoplastic dambreaks and the slump test

Y. Liu [a,*], N.J. Balmforth [a], S. Hormozi [b]

[a] Department of Mathematics, University of British Columbia, Vancouver, BC V6T 1Z2, Canada
[b] Department of Mechanical Engineering, Ohio University, Athens, OH 45701-2979, USA

ARTICLE INFO

Keywords:
Yield stress
Plasticity
Slump test
Volume of fluid
Regularization
Augmented-Lagrangian

ABSTRACT

We report computations of the axisymmetric slump of viscoplastic fluid using the volume-of-fluid (VOF) method. The constitutive law is dealt with by either regularization or the augmented-Lagrangian method. The interface is tracked by the PLIC scheme, modified in order to avoid resolution issues associated with the over-ridden finger of ambient fluid that results from the no slip condition and the resulting inability to move the contact line. Numerical results are compared with asymptotic analyses for shallow gravity currents or slender vertical columns. The critical yield stress for failure is computed and bounded analytically using plasticity methods. The simulations are compared with experiments either taken from existing literature or performed using Carbopol. The comparison is satisfying for lower yield stresses; discrepancies for larger yield stresses suggest that the mechanism of release may affect the experiments.

1. Introduction

Many fluids in industry or nature behave like viscoplastic fluids, including toothpaste, cement, mortar, foam, mud and mayonnaise. The crucial property of these materials is the yield stress, τ_Y, that must be breached in order for fluid to flow. If the imposed stresses fail to reach this threshold, the material remains solid-like, with any deformation often assumed small and discarded. In that situation, which underpins popular constitutive models such as the Bingham and Herschel–Bulkley laws, the stress state of the material becomes formally indeterminate [1]. Together with the need to track the boundaries of the yielded regions, this complicates significantly efforts aimed at theoretical modelling. Numerical strategies to overcome such difficulties have been developed in recent years and here we apply them to the particular problem of the axisymmetric slump of a yield-stress fluid under gravity.

Such collapses are exploited widely to gauge fluid rheology in the concrete, mineral and food industries. The slump test, for example, is commonly used to measure the yield stress of fresh concrete. In this test, a container filled with concrete is lifted to release the material and allow it to spread under gravity; at stoppage, the vertical distance over which the concrete falls, the "slump height", is measured as an indicator of yield stress. A number of experimental studies have been directed at establishing the precise relation of the slump height to the yield stress for a variety of different types of viscoplastic fluids [2–5].

Theoretical studies of the slump test have been performed using either numerical computations, asymptotic analysis suitable for the limit of shallow flow, or estimates and bounds based on plasticity theory [2,4,6–14]. The numerical simulations have been conducted using a variety of numerical techniques, although most of the algorithms employed were not specially designed to capture yield-stress rheology or carefully track fluid interfaces. The current status of the modelling of the slump test is reviewed by Roussel et al. [11].

One goal of the current article is to provide a reliable solution of the benchmark problem proposed in [11], and to offer a more complete description of the slump behaviour over a wider range of physical conditions. For the task, we perform computations based on the VOF method to deal with the fluid interface and exploiting specially designed codes to capture the yield-stress rheology. Our study follows on from an earlier one [15] in which we considered two-dimensional dambreaks of viscoplastic fluid. We complement the computations with asymptotic theory for shallow gravity currents and slender vertical columns, and bounds from plasticity theory to constrain the mode of failure for slumps near the critical yield stress whereat no collapse actually occurs.

A second goal is to compare our theoretical modelling with experiments, collating some of the existing measurements from the literature [2,3]. These experiments have not previously been performed sufficiently thoroughly to disentangle the effects of material rheology, the mechanism of release, and any interaction with the underlying surface (effective slip). Therefore, we also perform our own suite of experiments using aqueous suspensions of Carbopol. This suspension is often suggested to be well characterized by a Herschel–Bulkley rheology and potentially eliminates some of the confounding effects brought into experiments by non-ideal material behaviour [1]. We thereby provide a demanding test of the theory whilst gauging the effects of the release mechanism and any effective slip.

* Corresponding author.
E-mail address: yliu0218@math.ubc.ca (Y. Liu).

https://doi.org/10.1016/j.jnnfm.2018.04.012
Received 18 March 2018; Received in revised form 23 April 2018; Accepted 30 April 2018
Available online 1 May 2018

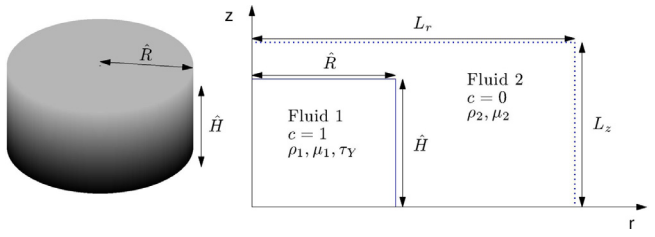

Fig. 1. Sketch of the geometry.

2. Formulation

2.1. Problem set-up and solution strategy

The geometry of the problem is shown in Fig. 1: we use an axisymmetric cylindrical polar coordinate system (r, z) to describe the sudden release of a cylinder of incompressible Bingham fluid with radius $\hat{R}$ and height $\hat{H}$. The fluid has density ρ_1, yield stress τ_Y and plastic viscosity μ_1 and is immersed in an ambient Newtonian fluid with density ρ_2 and viscosity μ_2. The density and viscosity ratios are set at the small values $\frac{\rho_2}{\rho_1} = \frac{\mu_2}{\mu_1} = 0.002$ in order to minimize the effects of the ambient fluid (we have verified that the precise values of these ratios have no significant effect on the computations once one deals with the resolution issues described in Section 2.3). We use the VOF method to track the fluid interface, which introduces an advected concentration field $c(r, z, t)$ to distinguish the fluid phase: $c = 1$ represents the viscoplastic fluid, and $c = 0$ denotes the Newtonian ambient. Given c, bulk material parameters are computed using linear interpolation. The initial configuration is

$$c(r, z, 0) = \begin{cases} 1 \text{ for } 0 \le r \le \hat{R}, 0 \le z \le \hat{H}, \\ 0 \text{ elsewhere.} \end{cases}$$

The two fluids are miscible, eliminating interfacial tension.

The computation domain extends to a height L_z and radius L_r, which are chosen to ensure that these boundaries remain remote and do not affect the evolution of the slump. We impose no slip $(u = 0, w = 0)$ on the bottom $z = 0$, regularity conditions on the axis $r = 0$ (*i.e.*$u = \partial w/\partial r = 0$), and no normal flow and free slip conditions along $r = L_r$ and $z = L_z$.

We use two methods to deal with the yield-stress constitutive law: a regularization scheme that treats the unyielded region as a highly viscous fluid, and an augmented-Lagrangian scheme that explicitly treats the yield stress within a weak formulation of the problem [16,17]. Both are implemented in C++ as an application of the PELICANS platform (*e.g.* [18]).

2.2. Dimensionless model equations

We scale lengths by the initial height $\hat{H}$, velocities by the speed scale $U = \rho_1 g\hat{H}^2/\mu_1$, and time by $\hat{H}/U$, where g is the gravitational acceleration; the stresses and pressure are scaled by $\rho_1 g\hat{H}$. The governing equations for the concentration field c, velocity $\boldsymbol{u} = (u, w)$, deviatoric stress tensor $\boldsymbol{\tau}$, and pressure p are then

$$\begin{aligned} &\nabla \cdot \boldsymbol{u} = 0, \qquad \frac{\partial c}{\partial t} + (\boldsymbol{u} \cdot \nabla)c = 0, \\ &\boldsymbol{\rho} Re\left[\frac{\partial \boldsymbol{u}}{\partial t} + (\boldsymbol{u} \cdot \nabla)\boldsymbol{u}\right] = -\nabla p + \nabla \cdot \boldsymbol{\tau} - \boldsymbol{\rho}\begin{pmatrix} 0 \\ 1 \end{pmatrix}, \end{aligned} \tag{1}$$

where

$$\boldsymbol{\rho} = c + (1 - c)\frac{\rho_2}{\rho_1} \qquad \text{and} \qquad \mu = c + (1 - c)\frac{\mu_2}{\mu_1}. \tag{2}$$

The unregularized Bingham constitutive law, used in the augmented-Lagrangian method, is

$$\begin{cases} \dot{\gamma}_{jk} = 0, & \tau < cB, \\ \tau_{jk} = \left(\mu + \dfrac{cB}{\dot{\gamma}}\right)\dot{\gamma}_{jk}, & \tau > cB, \end{cases} \tag{3}$$

whereas the regularization method uses the variant,

$$\tau_{jk} = \left(\mu + \frac{cB}{\dot{\gamma} + \epsilon}\right)\dot{\gamma}_{jk}, \tag{4}$$

where $\tau = \sqrt{\frac{1}{2}\sum_{j,k}\tau_{jk}^2}$ and $\dot{\gamma} = \sqrt{\frac{1}{2}\sum_{j,k}\dot{\gamma}_{jk}^2}$ denote second tensorial invariants, and the deformation rates are given by

$$\begin{pmatrix} \dot{\gamma}_{rr} & \dot{\gamma}_{r\theta} & \dot{\gamma}_{rz} \\ \dot{\gamma}_{\theta r} & \dot{\gamma}_{\theta\theta} & \dot{\gamma}_{\theta z} \\ \dot{\gamma}_{zr} & \dot{\gamma}_{z\theta} & \dot{\gamma}_{zz} \end{pmatrix} = \begin{pmatrix} 2u_r & 0 & u_z + w_r \\ 0 & 2u/r & 0 \\ u_z + w_r & 0 & 2w_z \end{pmatrix}, \tag{5}$$

with subscripts represent partial derivatives, except in the case of tensor components. The scalings introduce the dimensionless initial radius (or aspect ratio), and the Reynolds and Bingham numbers,

$$R = \frac{\hat{R}}{\hat{H}}, \qquad \text{Re} = \frac{\rho_1 U\hat{H}}{\mu_1} \qquad \text{and} \qquad B = \frac{\tau_Y\hat{H}}{\mu_1 U}. \tag{6}$$

The regularization parameter ϵ in (4) is taken to be 10^{-8}, which was verified to be sufficiently small that the modification of the constitutive law had an insignificant effect on the results reported below (but see the comment at the end of Section 2.3). Given the concentration field, we define the instantaneous position of the surface of the slump to be given by $c(r, z = h) = \frac{1}{2}$. For most of the computations, we select parameters so that inertial effect is small, $\text{Re} = 10^{-3}$, and vary B and R.

2.3. PLIC Scheme with interface correction

The piecewise-linear-interface-construction (PLIC) [19,20] is a contemporary standard in the VOF method. The interface is represented by a line segment in each grid cell, which is computed using the volume fraction c, as in [19]. Then, given the velocity field, the line segment is advected to a new position, and c updated accordingly. In view of the boundary conditions, there is no flux of c into or out of the domain, which is incorporated into the scheme in the manner in which the solver advects c along the boundary. Importantly, the bottom boundary is no slip, which does not permit the contact line to move and introduces an awkward resolution issue, as in the 2D problem in [15]. More specifically, as the viscoplastic fluid collapses and spreads out, a finger of ambient fluid adhering to the bottom surface is over-ridden. For the relatively low density and viscosity ratios that we employ, this finger lubricates the slumping viscoplastic current and thins dramatically to introduce the resolution issue [15]. A key problem is that the scheme fails to accurately evolve c when the interface is inside the lowest grid cell, leaving the finger artificially thick and lubricating.

A common way of moving the contact line in problems with surface tension and Newtonian fluid is to replace the boundary condition with another that permits slip. However, numerical solutions may not converge with mesh refinement [21]. Instead, in [15] we suggested a correction scheme that eliminates the finger in a different way, allowing the computations to remain well resolved over long times. The main point is that, with no slip, a finger of ambient fluid must still coat the underlying surface. However, counter to the un-corrected VOF scheme, the finger actually becomes too thin to lubricate the slump and should instead be ignored. Practically, the scheme implements this idea by removing all the ambient fluid from a grid cell adjacent to the base when c exceeds a threshold near unity (chosen to be 0.99). This procedure clips the interface when it invades the lowest grid cells, thereby truncating the finger and rendering the computation convergent in grid spacing [15].

Despite the success of the scheme for 2D dambreaks, the algorithm is not conservative, with the mass of viscoplastic fluid growing with time. This awkward feature does not impair computations in 2D, but it does become more problematic in axisymmetric geometry, for which the convergence of the solutions with mesh refinement is weakened. For the current computations we therefore modified the correction scheme so that it conserved mass. In particular, whenever a correction to c was implemented, and some of the ambient fluid removed from the one of the lowest grid cells, the lost material was added back by uniformly redistributing it into the grid cells containing the interface (where $c = \frac{1}{2}$).

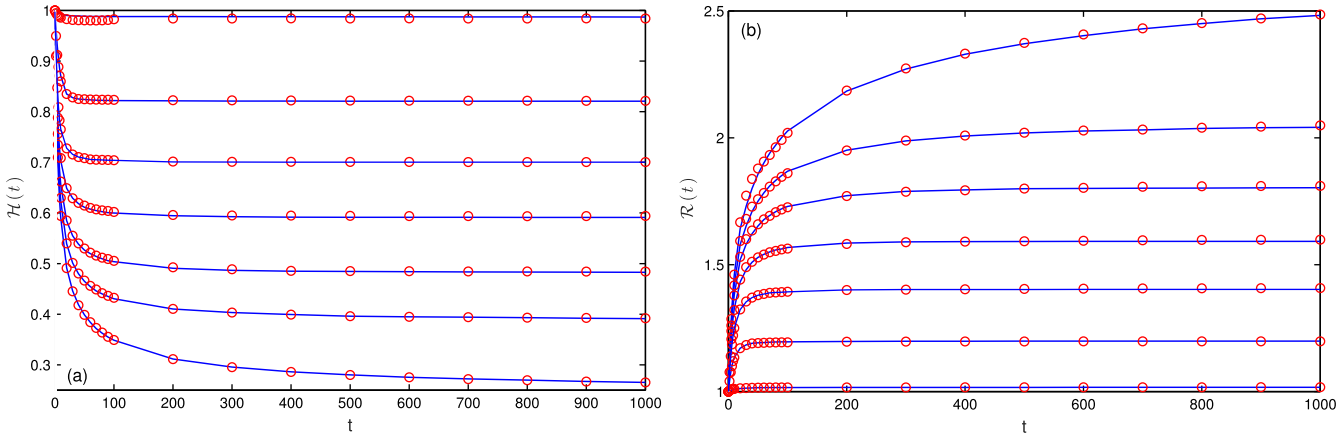

Fig. 2. Time series of flow height $\mathcal{H}(t)$ and front position $\mathcal{R}(t)$ for Bingham slumps with $R = 1$ and $B = 0.01$, 0.03, 0.05, 0.08, 0.125, 0.2 and 0.3. Blue curves are from regularization, and red circles from the augmented-Lagrangian method (For interpretation of the references to color in this figure legend, the reader is referred to the web version of this article.).

Essentially, this redistribution incurs an error in the position of the interface that is of the order of a small fraction of the grid spacing, but in such a way that mass is conserved. Though hard to justify from a physical perspective, the resulting **conservative correction scheme** converges more satisfyingly with mesh refinement for slumps with Newtonian fluid than the original **non-conservative scheme** (see Appendix A), chiefly because the latter suffers a resolution-dependent mass loss.

The conservative correction scheme also performs better for Bingham fluid using either the regularized constitutive law or the augmented-Lagrangian solver. Moreover, both produce comparable results for the global properties of the slumps (see, for example, Fig. 2 below), and their interaction with the PLIC scheme does not introduce any additional unexpected issues. In more detail, the regularization scheme has the drawback that the fluid can never truly come to rest and can fail to correctly predict the positions of the yield surfaces [22]. However, the regularization scheme is faster than the augmented-Lagrangian code. Therefore, we use regularization scheme for exploring global features of the slumps (defining the flow to have come to rest when $\mathrm{Max}(|\boldsymbol{v}|) < 10^{-5}$), while for the finer details such as the yield surfaces, we compare both schemes.

3. Bingham slumps

Fig. 2 shows the slumps of cylinders of Bingham fluid for $R = 1$ and varying yield stress B. Displayed is the central depth $\mathcal{H}(t)$ along with the radial position of the flow front $\mathcal{R}(t)$ (defined as the largest radial extent of the interface, $c = \frac{1}{2}$). The computations suggest that flow is arrested in finite time and illustrate how collapse only occurs when the yield stress is below a critical value B_c. A selection of the final profiles is illustrated in Fig. 3(a).

Further details of the phenomenology of a slump are shown in Fig. 4. Initially, the stresses exceed the yield value throughout the cylinder except over a small conical region at its core. Fluid subsequently slumps outwards, reducing the stresses and allowing that plug to expand with time. Eventually, stresses decline towards B all the way to the flow front, bringing the fluid to rest. Note that, there is only a single central plugged region; for equivalent two-dimensional dambreaks [15] plugs persist at the periphery of the initial configuration, leading to sharp corners that decorate the final deposit. Rigid features of this sort cannot occur in axisymmetric slumps because the fluid edge must expand in order to fall. However, analogous weakly yielded zones persist during the collapse, then plug up to create sharp rings that disfigure some of the final shapes (see Fig. 3).

As for 2D dambreaks [15], when the initial configuration is sufficiently wide, fluid only collapses near the edge, leaving an unyielded

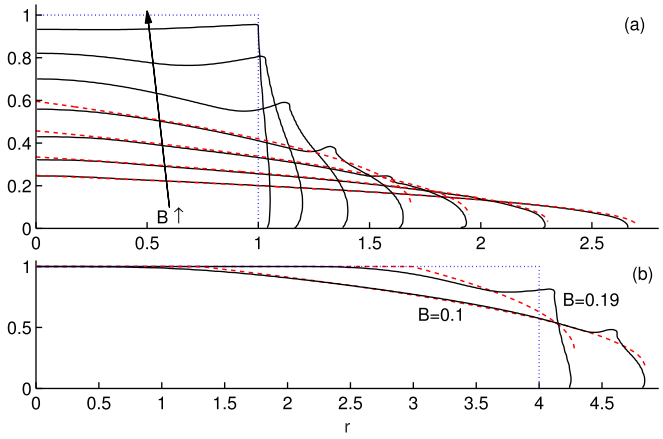

Fig. 3. Profiles of the final deposit of cylindrical slumps with (a) $R = 1$, $B = 0.01$, 0.02, 0.04, 0.07, 0.125, 0.2 and 0.275, and (b) $R = 4$, $B = 0.1$ and 0.19. The solid curves show numerical computations, the dashed curves show the improved shallow-layer asymptotic result in (11) (for the lowest four values of B in (a)), and the dotted lines show the initial cylinders.

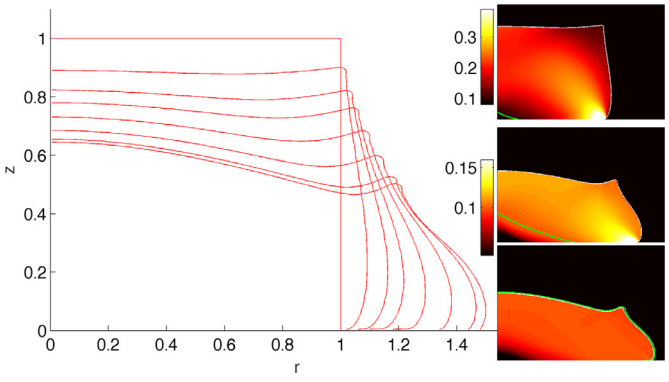

Fig. 4. Evolution of the interface for a slumping cylinder with $(R, B) = (1, 0.1)$. The main panel shows the interface at the times $t = 0$, 2, 4, 6, 8, 20, 200 and 1000. The three insets show the stress invariant τ as a density on the (r, z)–plane for the times $t = 2$, 20 and 1000 (with a common scale for the last two cases). The green curve shows the yield surface. (For interpretation of the references to color in this figure legend, the reader is referred to the web version of this article.)

flat-topped central section. Such "incomplete slumps" arise when the central plug spans the entire fluid layer and are illustrated in Fig. 3(b).

3.1. Shallow flow

When flow is shallow and inertia is negligible, lubrication theory can be applied to obtain analytical results [12]. With our current scaling of the problem, this limit is achieved when $B \ll 1$. To account for the low aspect ratio, we rescale the horizontal coordinate $r = \epsilon^{-1}\chi$, deviatoric stress components $\tau_{ij} = \epsilon\check{\tau}_{ij}$ and Bingham number $B = \epsilon\check{B}$ using a small parameter $\epsilon \ll 1$, and then restate the force balance equations for the viscoplastic layer:

$$\begin{cases} -p_\chi + \dfrac{\epsilon}{\chi}(\chi\check{\tau}_{rr})_\chi - \dfrac{\epsilon}{\chi}\check{\tau}_{\theta\theta} + \check{\tau}_{rz,z} = & 0, \\ -p_z + \dfrac{\epsilon^2}{\chi}(\chi\check{\tau}_{rz})_\chi + \epsilon\check{\tau}_{zz,z} = & 1. \end{cases} \tag{7}$$

Neglecting the ambient fluid, the surface of the current can be located by the elevation $z = h(\chi, t)$, and is force free, demanding that

$$\left.\begin{array}{l} \check{\tau}_{rz} + h_\chi(p - \epsilon\check{\tau}_{rr}) = 0 \\ p - \epsilon\check{\tau}_{zz} + \epsilon^2 h_\chi\check{\tau}_{rz} = 0 \end{array}\right\} \quad \text{at } z = h. \tag{8}$$

At leading order, we find that $p \sim h - z$ and $\check{\tau}_{rz} \sim -h_\chi(h - z)$. The constitutive law and depth-integrated continuity equation can then be used to derive an evolution equation for $h(\chi, t)$ [12,23]. However, the final profile arises when radial spreading speeds subside and $\check{\tau}_{rz} \to \check{B}$ at the base of the fluid layer $z = 0$. Thence $\check{\tau}_{rz}(\chi, 0) \sim -hh_\chi \sim \check{B}$, which gives

$$h(r) \sim \sqrt{2B(r_\infty - r)}, \tag{9}$$

in terms of the original variables, where r_∞ is the final radius.

In [15] a higher-order approximation for the final profile of a 2D slump was developed by continuing the asymptotic solution to $O(\epsilon)$, assuming that $\check{\tau} \to \check{B}$ throughout the fluid layer. We follow suit here, although a significant complication emerges owing to the axisymmetric geometry. In particular, in addition to the two force balance equations, we must also satisfy

$$\begin{cases} \check{\tau}_{rr} + \check{\tau}_{\theta\theta} + \check{\tau}_{zz} = 0 \\ \dfrac{1}{2}\left(\check{\tau}_{rr}^2 + \check{\tau}_{\theta\theta}^2 + \check{\tau}_{zz}^2\right) + \check{\tau}_{rz}^2 = \check{B}^2, \end{cases} \tag{10}$$

leaving us one equation short for determining the full stress state (*i.e.* we have four equations for the five unknowns p, $\check{\tau}_{rr}$, $\check{\tau}_{\theta\theta}$, $\check{\tau}_{rz}$ and $\check{\tau}_{zz}$). The origin of this indeterminacy is the component $\check{\tau}_{\theta\theta}$, which does not arise in 2D and highlights how the stress field cannot, in general, be constructed independently of the velocity field. The situation is identical to classical plasticity theory where the so-called von Karman–Haar hypothesis is often invoked to avoid this problem. The hypothesis, which states that $\check{\tau}_{\theta\theta}$ must equal one of the principal stresses in the (r, z)–plane, implies that $\check{\tau}_{\theta\theta}^2 \equiv \frac{1}{3}\check{B}^2$ [24]. However, $\check{\tau}_{rz}^2 \to \check{B}^2$ at $z = 0$ for the leading order lubrication solution, indicating that $\check{\tau}_{\theta\theta}$ must vanish at the base of the fluid layer. Therefore, the von Karman–Haar hypothesis contradicts the leading-order asymptotic solution and cannot be invoked here.

Instead, we add the approximation $\check{\tau}_{rr} \sim \check{\tau}_{\theta\theta}$, which is suggested by both the velocity field of the leading-order asymptotic solution and the numerical computations; see Appendix B. With this alternative hypothesis, the asymptotic analysis can be continued to $O(\epsilon)$ in order to arrive at the higher-order asymptotic approximation,

$$h(r) \sim \sqrt{2B(r_\infty - r)} + \frac{\sqrt{3}}{4}\pi B \tag{11}$$

(again in terms of the original variables).

The predictions in (9) and (11) are compared to a numerical simulation for a slump with $B = 0.0074$ and $R = 0.2546$ in Fig. 5. Fig. 3 also compares the improved approximation (11) with computed final shapes over a wider range of B. Note that (11) predicts that the final profile ends in a vertical cliff, violating the shallow-layer asymptotics. Nevertheless, (11) provides a meaningful prediction along the flow body that furnishes a better approximation than the leading order result (9), even when the flow is not particularly shallow ($B > 0.04$).

In the example of Fig. 5, the fluid yields significantly almost everywhere, removing any sign of the initial shape in the final profile. Indeed, computations that begin with the same amount of fluid but conical initial shape also lead to similar final profiles. Fig. 5 includes a computation using an initial cone with a top radius of $R_{\text{top}} = 1/6$ and bottom radius of $R_{\text{base}} = 1/3$, which corresponds to the ASTM standard geometry; the final state cannot be distinguished from that of the cylindrical dambreak in the plot. Thus, the example shown in this figure corresponds to the benchmark problem proposed in [11]. Indeed, on the right-hand side of the figure, the profiles are replotted in dimensional variables using $\hat{H} = 30$ cm; the results can then be directly compared with Fig. 5 in [11].

The agreement amongst the computations in [11] is relatively poor, a discrepancy that may arise from different treatments of the contact line and the fluid rheology. By contrast, the current computations align satisfyingly with (11), have converged with respect to mesh refinement, and are independent of the numerical algorithm (augmented-Lagrangian or regularization). Our computation indicates that the final (dimensional) radius is 28 cm, in comparison to the average of 29.5 cm quoted in [11]. Fig. 5 also tells the cautionary tale of the results when we fail to resolve the finger of upper-layer fluid by applying the uncorrected PLIC scheme, or overly regularize the constitutive model. Both deficiencies lead to an enhancement in spreading. Note that there is essentially no effect of inertia on the profiles shown in Fig. 5: recomputing the results with a Reynolds number based on the benchmark conditions, rather than the artificially low value used for the bulk of our simulations, leads to no significant differences.

When a complete slump does not occur but a central section of the initial cylinder survives, the shallow-layer solution is modified accordingly:

$$h = \begin{cases} 1, & 0 < r < r_\infty - \dfrac{1}{2B} \\ \sqrt{2B(r_\infty - r)} + \dfrac{\pi\sqrt{3}}{4}B, & r_\infty - \dfrac{1}{2B} < r < r_\infty \end{cases} \tag{12}$$

This approximation is again compared with numerical final shapes in Fig. 3(b).

3.2. Slender columns

For a tall slender column ($R \ll 1$), the asymptotic analysis of [15] can be generalized to determine the instantaneous radius $r = r(a, t) \ll 1$ in terms of a Lagrangian coordinate $a \in [0, 1]$ corresponding to initial height: where the fluid is locally yielded, we find

$$\begin{cases} r^2(a,t) = E(t)r_0^2(a) + \dfrac{1 - E(t)}{\sqrt{3}B}\displaystyle\int_a^1 r_0^2(x)dx \\ z(a,t) = \displaystyle\int_0^a \frac{r_0^2(x)}{r^2(x,t)}dx, \qquad E(t) = e^{-\frac{Bt}{\sqrt{3}}}, \end{cases} \tag{13}$$

where $r_0(a)$ represents the shape of the initial column. As $t \to \infty$, we then obtain

$$\begin{cases} r^2(a) = \dfrac{1}{\sqrt{3}B}\displaystyle\int_a^1 r_0^2(x)dx, \\ z(a) = \sqrt{3}B\ln\left[\dfrac{\int_0^1 r_0^2(x)dx}{\int_a^1 r_0^2(x)dx}\right]. \end{cases} \tag{14}$$

The solution in (13) and (14) must be matched to a plugged upper section of the column, which always remains unyielded. The yield surface is given by $r_0(a_Y) = r(a_Y)$. The dimensionless slump height s (the difference between the initial and final heights) is therefore

$$s = a_Y + \sqrt{3}B\ln\left[\frac{\sqrt{3}Br_0^2(a_Y)}{\int_0^1 r_0^2(a)da}\right]. \tag{15}$$

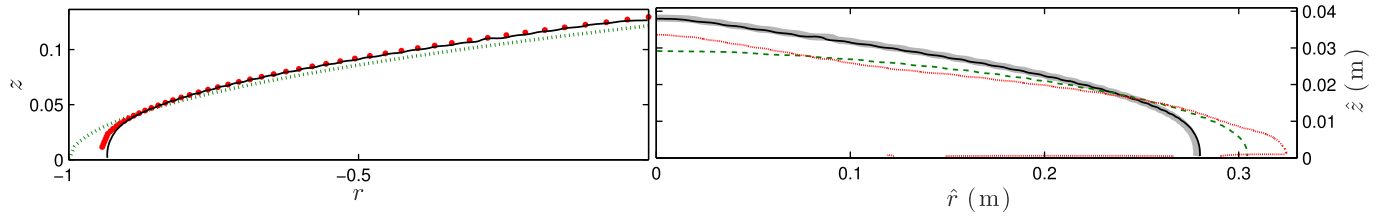

Fig. 5. Final profile for a cylindrical dambreak with $B = 0.0074$ and $R = 0.2546$. The thin black curve shows the numerical simulation. On the left, the data is plotted using dimensionless variables, and the leading-order and improved asymptotic predictions in (9) and(11) are included as the dotted (green) line and (red) points, respectively. On the right, the data is replotted in dimensional variables assuming $\hat{H} = 0.3$ m. Also shown are three other final profiles: one from a simulation beginning with a cone with the same volume, with a top radius of $R_{\text{top}} = 1/6$ and bottom radius of $R_{\text{base}} = 1/3$ (the ASTM standard geometry; thick light grey line); a second from a simulation with the regularized Bingham model in which the regularization parameter is increased to 10^{-4} (dashed line); and a third from a simulation that does not apply the interface correction scheme to remove the underlying finger of ambient fluid (thin red contour) (For interpretation of the references to color in this figure legend, the reader is referred to the web version of this article.).

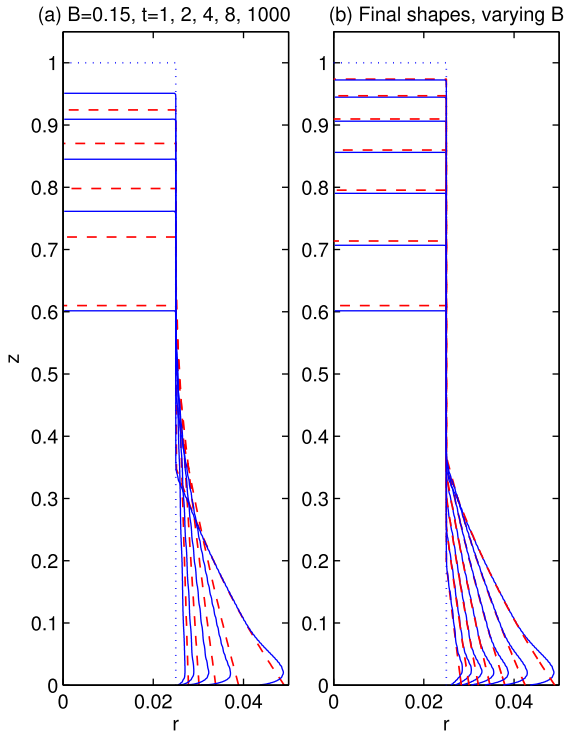

Fig. 6. (a) Collapse of a cylindrical column with $B = 0.15$, showing the interface at the times indicated. (b) Final shapes of cylinder with $R = 0.025$ and $B = 0.15$, 0.20, 0.25, 0.30, 0.35, 0.40 and 0.45. Dashed lines indicate the slender asymptotic predictions (13) and (14); solid lines are from numerical simulations.

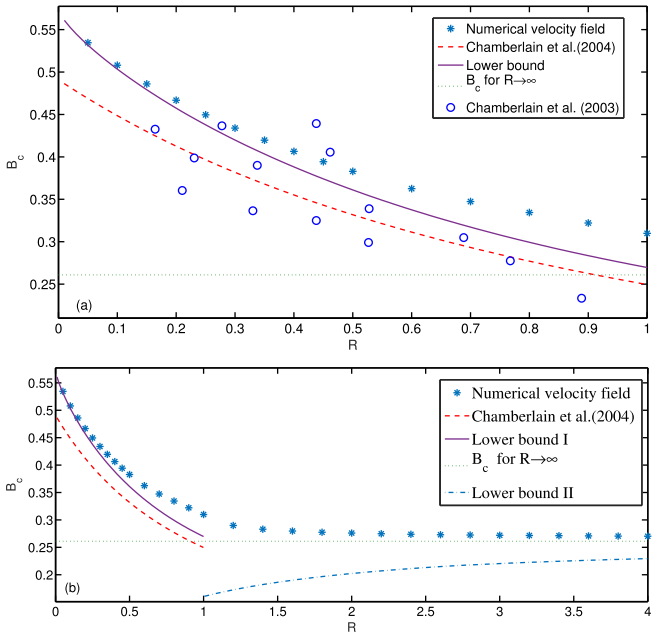

Fig. 7. Critical yield stress for collapse, B_c, as a function of initial radius R. Blue stars indicate the results from numerical simulations; the solid line shows the lower bound assuming a mechanism involving basal collapse (labelled I); the dotted line shows the result from [14]. In (a) we show the range $R < 1$ and include experimental data from [27]. In (b) we show the range $R < 4$ and an alternative lower bound assuming a peripheral collapse (labelled II) (For interpretation of the references to color in this figure legend, the reader is referred to the web version of this article.).

For an initial cylinder, $r_0(a) = R$, and

$$s = 1 - \sqrt{3}B + \sqrt{3}B\ln(\sqrt{3}B), \tag{16}$$

which is widely used as a prediction of the slump test [2]. This immediately implies that the column will not yield anywhere if $B > B_c = 1/\sqrt{3} \approx 0.577$.

Fig. 6 compares numerical computations with the slender-column asymptotics for initial shape with $r_0(a) = R = 0.025$. First, the dynamical evolution of a column with $B = 0.15$ is shown; second, the final shape is compared for cases with varying yield stress B. Note that undulations in the surface profile do not appear near the base of the column in the axisymmetric simulations, unlike in 2D [15]. As a result, the computations and slender-column theory agree more satisfyingly, except at the very base of the column where the no slip condition is not correctly captured by the asymptotics.

3.3. Failure mode

Just below the critical value $B_c(R)$ for which no slump will occur, the collapse is characterized by a particular mode of failure that depends on the initial shape. To compute the critical yield stresses and find the failure modes, we use the augmented-Lagrangian method and monitor the rate at which the iterations of the scheme converge during short-time computations ending at $t = 1$; iterations converge significantly faster when $B > B_c$. The results are plotted in Fig. 7. As $R \to 0$, B_c converges to $1/\sqrt{3}$, the limit for a slender column; as $R \to \infty$, B_c approaches the value 0.265, corresponding to the failure of a 2D vertical embankment [25,26].

Fig. 8 collects together computational results for sample failure modes, extracted from the initial velocity field for simulations with $B \approx B_c$. Much as expected on physical grounds and found for 2D dambreaks, the fluid collapses by failing first over a basal region for thinner initial cylinders, and only at the periphery with a wider ini-

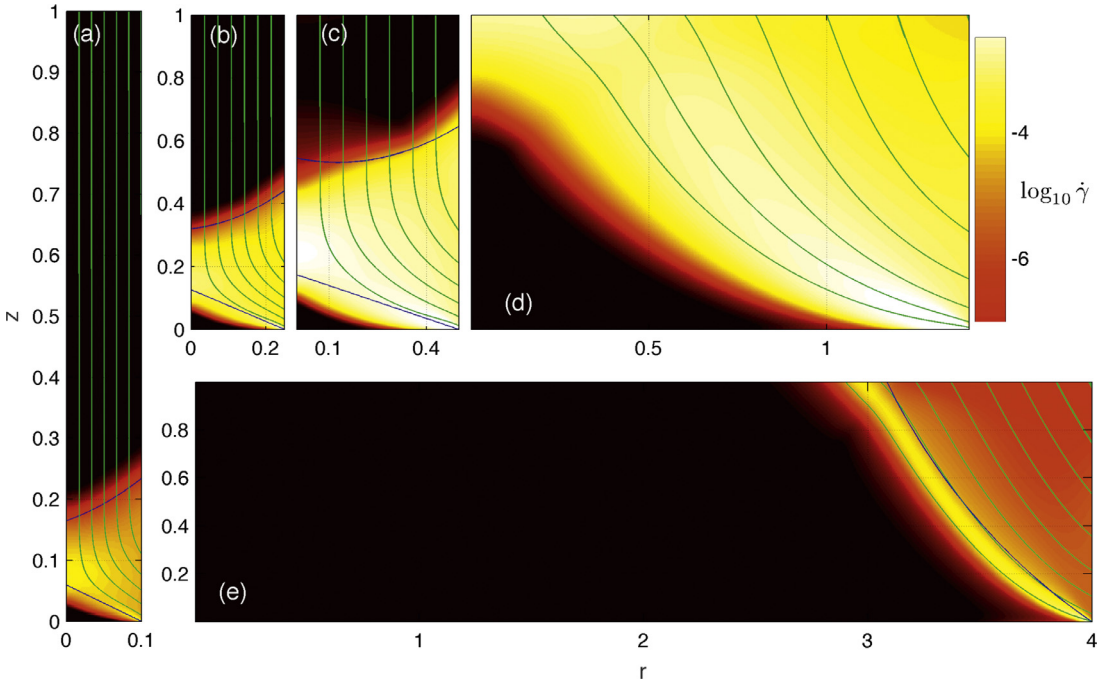

Fig. 8. Strain-rate invariant plotted logarithmically as a density on the (r, z) plane for solutions with $B \approx B_c$, $Re \approx 0$, $t \approx 0$, at the values of R indicated by the r-axis limits. Also shown are a selection of streamlines. In $(a) - (c)$, the solid blue lines indicate the border of the plastic region predicted by limit analysis (17). In (e), the blue line indicates the circular failure surface of the lower bound solution in 2D geometry [15] (For interpretation of the references to color in this figure legend, the reader is referred to the web version of this article.).

tial state; cylinders with radii around unity show mixed types of failure modes.

The critical yield stress can be bounded using methods from plasticity theory [28]. In particular, lower bounds on B_c can be established by maximizing

$$\mathcal{B} = \frac{\iint w r dr dz}{\iint B\dot{\gamma} r dr dz}, \tag{17}$$

over families of trial velocity fields. Guided by the numerical failure modes in Fig. 8, we find a lower bound for slender initial cylinders by considering trial velocity fields that are composed of a rigid central section in $z < f(r)$, an overlying descending plug for $z > g(r)$, and a plastically deforming region sandwiched in between. We take the "yield surfaces" $f(r)$ and $g(r)$ to have parabolic shape and the (incompressible) plastic deformation to have a cubic horizontal velocity profile. Thus, our trial is

$$\boldsymbol{v} = \begin{cases} (0,-1) & g(r) < z < 1 \\ (u,w) & f(r) < z < g(r) \\ (0,0) & 0 < z < f(r) \end{cases} \tag{18}$$

with

$$\begin{cases} u = \dfrac{6r}{g(r)-f(r)}\eta(1-\eta)^2 \\ w = -(6-8\eta+3\eta^2)\eta^2 - 6r\eta(1-\eta)^2\eta_r \\ \eta = \dfrac{z-f(r)}{g(r)-f(r)} \end{cases} \tag{19}$$

Optimization of $\mathcal{B}$ can then be performed over the parameters c_j of the parabolas defining $f = c_1(R-r) + c_2(R-r)^2$ and $g = c_3 + c_4(R-r) + c_5(R-r)^2$.

Upper bounds on B_c can also be constructed using trial admissible stress fields [28]. However, in axisymmetric geometry, without a velocity field to determine all the stress components, an additional assumption is needed such as the von Karman–Haar hypothesis. This artifice permitted Chamberlain et al. [29] to construct upper bounds on B_c. Unfortunately, this hypothesis is not appropriate for our axisymmetric slump and so their upper bound does not apply here.

Note that the trial velocity field in (19) is continuous across the curves $z = f(r)$ and $g(r)$, in line with the structure of the failure modes of Fig. 8. This contrasts sharply with the 2D problem in which failure can occur over distinct curves that support velocity jumps and which become smoothed into viscous boundary layers in numerical solutions. Indeed, Chamberlain et al. [14] have previously computed bounds for the failure of cylinders using trial velocity fields more similar to the 2D failure modes. However, distinct failure lines and viscous boundary layers do not characterize our axisymmetric solutions, leading to the choice of the cubic velocity field in (19). This choice complicates the optimization computation but significantly improves the results.

The lower bound on B_c for basal failure is included in Fig. 7, and compares well with numerical computations when R is small. Fig. 8 also displays the predictions of the optimization calculation for the surfaces $z = f(r)$ and $g(r)$, which have some correspondence with the computed yield surfaces. For larger values of R, the bound diverges from the computations and the trial velocity field is less similar to the actual failure modes. Both occur because of the switch in the form of the failure mode, from a basal collapse to a peripheral one.

For a lower bound on B_c for peripheral failure we require a different trial velocity field. In 2D, a useful bound is found by assuming that a circular arc of failure connects the foot of the vertical face at the edge with some point on the top surface; above this arc, material rotates rigidly out of initial position. For a simple axisymmetric generalization of this trial, we again assume that a circular arc of failure arises, but divide the 2D velocity field by r (with the horizontal coordinate x replaced by r), which ensures that the trial is incompressible. The resulting bound is shown in Fig. 7, and always lies below the 2D bound (though converges to it for $R \to \infty$).

4. Comparison with experiments

4.1. Methods

To complement the theory, we performed experiments using an aqueous suspension of Carbopol Ultrez 21 (with a concentration of about

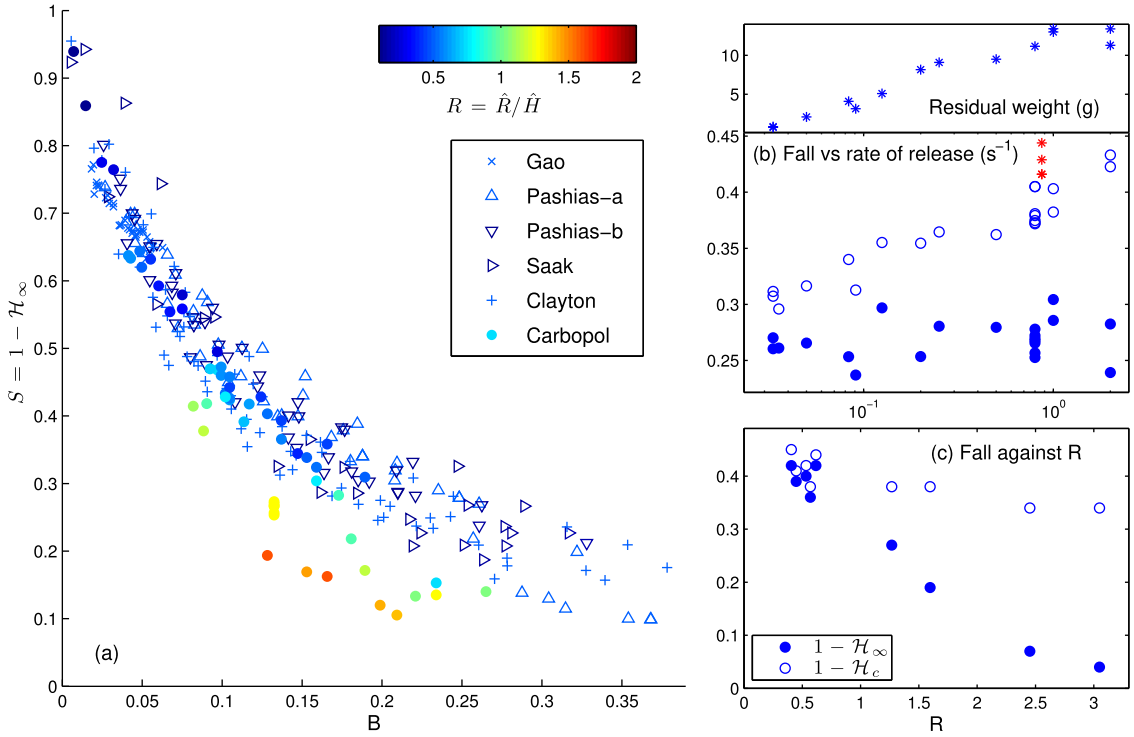

Fig. 9. (a) Comparison of experimental slump height with previously published data for $R < 2$. The points are colour coded by R, as indicated by the colour bar. The published data is taken from [5] (Gao; $R = \frac{1}{2}$), [2] (Pashias-a: data at $R \approx \frac{1}{2}$ for differing materials; Pashias-b: data for red mud with varying R), [3] (Saak; $R = 0.52$) and [4] (Clayton; $R = \frac{1}{2}$). On the right, slump height is plotted against (b) the rate of release (*i.e.* the inverse of the time taken to lift up the cylinder) for $\hat{R} = 3$ cm and $\hat{H} = 3.8$ cm, and (c) R for $\hat{H} \approx 3.1$ cm. Most slumps were conducted by releasing the fluid over about a second, but not recording the time precisely; several repeated slumps with this protocol are plotted at release rate 1.25 s^{-1}. In (b) and (c) the fall of the corner of the initial cylinder $1 - \mathcal{H}_c$ is also recorded (open circles). Panel (b) also shows the residual mass attached to the cylinder after the release of the fluid, and data for slumps that were conducted over a smooth surface (red stars; in these cases the slumps were left to come to rest for five minutes) (For interpretation of the references to color in this figure legend, the reader is referred to the web version of this article.).

0.5% by weight, and neutralized by sodium hydroxide). A Herschel–Bulkley fit to the flow curve measured in a rheometer (MCR501, Anton Paar, with roughened parallel plates) gave $\tau_Y = 39$ Pa, $n = 0.3$ and $K = 32$ Pa s^n.

Slump tests were conducted by filling a variety of cylinders with different geometry with the suspension, smoothing the fluid's upper surface with a sharp edge. The cylinders, with radii varying from 10 to 95 mm and heights over the range of 11 to 562 mm, were attached to a pivoted arm that raised each container in a relatively controlled and reproducible fashion. For most of the tests, the arm was raised relatively quickly, releasing the fluid over a time of about 1 s, and the surface over which the fluid slumped was a plexiglass plate roughened with sandpaper. Measurements of the final deposit were taken after waiting for a few minutes. However, we also conducted tests in which we varied the rate at which the cylinder was raised, or replaced the roughened plexiglass with either a smooth sheet or covered it with 60 grit sandpaper. Note that for the smaller aspect ratio cylinders that we used ($R < \frac{1}{2}$), there was a tendency for the slumps to topple over sideways if the cylinder was not raised sufficiently slowly (which typically lengthened the release time to a couple of seconds), highlighting an instability of tall thin columns [30]. We abandoned any tests that showed substantial sideways motion.

To remove the effect of the manner in which the fluid was released, we conducted a second series of extrusion experiments. Here, the Carbopol was pumped up onto the surface through a vent with a diameter of about 0.5 mm. For both the slump tests and extrusions, thickness profiles $h(r, t)$ were extracted by taking photographs from the side, allowing measurements of the final central height and radius (except for the extrusions over the smooth surface, as discussed below, the tests were axisymmetric).

Note that, for the slump tests, we continue to use the Bingham model to provide theoretical solutions to compare against the experiments, despite the fact that the Carbopol is better fitted by the Herschel–Bulkley law. Thus, we implicitly assume that the power-law viscosity plays a minor role in controlling the form of the final state of a slump. We explicitly confirmed this for isolated examples of dambreak computations in which we implemented the Herschel–Bulkley model with a power-law index suggested from the flow curve of the Carbopol (*i.e.* $n = 0.3$, see the end of Section 4.2 and Fig. 12). In order to improve the comparison with experiments, we also used this alternative rheological model for our computations of time-dependent extrusions. Specifically, the computations exploited the regularization,

$$\tau_{jk} = \left[c\dot{\gamma}^{n-1} + \frac{\mu_2}{\mu_1}(1 - c) + \frac{cB}{\dot{\gamma} + \epsilon} \right] \dot{\gamma}_{jk}. \tag{20}$$

The characteristic velocity scale in this case is given by $U = (\rho g \hat{H}^{n+1}/K)^{1/n}$ ($\rho = 10^3$ kg m^{-3}, $g = 9.81$ m s^{-2}).

4.2. Cylindrical dambreaks

The conventional slump test focuses on the distance fallen at the centre of the fluid, the so-called slump height $S = 1 - \mathcal{H}_\infty$, where $\mathcal{H}_\infty$ is the final central depth. A summary of our results for this diagnostic is presented in Fig. 9. An important experimental parameter that we varied in the current suite of experiments is the aspect ratio of the cylinder, $R = \hat{R}/\hat{H}$. Most previous experiments have conducted tests with aspect ratios close to a half, concluding that this parameter has little significant effect. However, the theoretical results summarized in Section 3 clearly expose how R plays an important role if varied over a sufficiently wide range. This is confirmed in our experiments, which clearly demonstrate

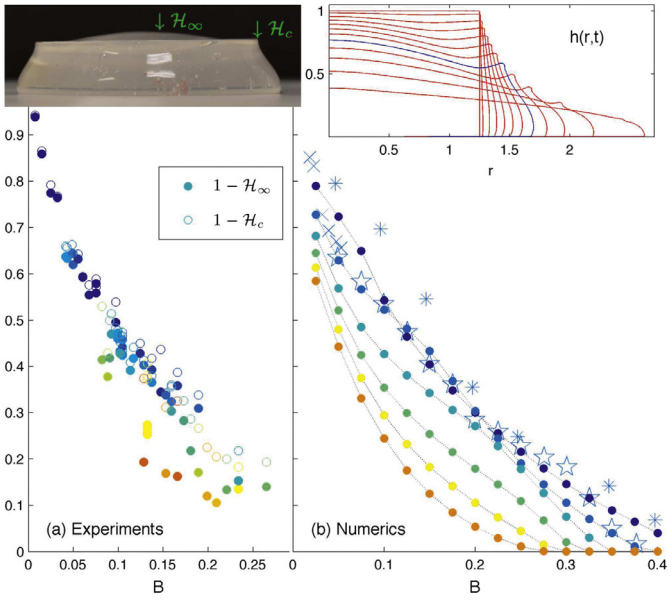

Fig. 10. (a) Experimental and (b) numerical slump heights against B for $R<2$. Shown in (a) are both S (filled circles) and the distance fallen by the corner of the initial cylinder $1-\mathcal{H}_c$ (open circles), as illustrated by the experimental image for $(R, B)\approx(1.25, 0.13)$ inset above (a) (and also shown in Fig. 12). Inset above (b) are the final profiles (red) of the computations with $R=1.25$; that matching the value of B of the experiment is highlighted (blue). The colour coding of the points by R is the same as in Fig. 9, and a collection of previous data (with $R=\frac{1}{2}$) from numerical computations are also plotted in (b) (crosses [5]; stars [7]; pentagrams [13]). (For interpretation of the references to color in this figure legend, the reader is referred to the web version of this article.).

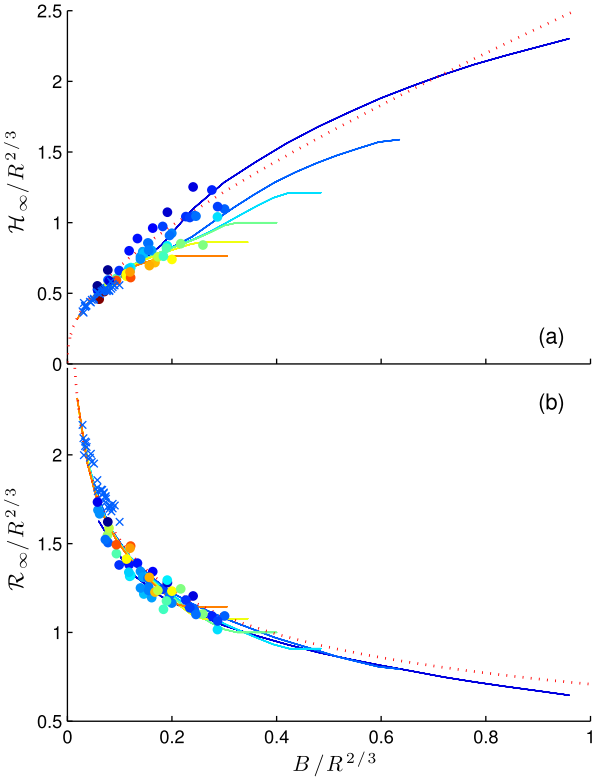

Fig. 11. The central depth and radius of the final deposit against Bingham number, all scaled by $R^{2/3}$, for $R<4$. Our results for Carbopol slumps are shown by the filled circles; the crosses show data from [5]. The results from the numerical simulations also plotted in Fig. 10 are shown by the solid lines; the improved asymptotic prediction from (11) is shown by the dotted line. The colour coding by R is the same as in Fig. 9.

how S decreases with R at fixed B; see the colour coding of the points in panel (a), and the plot for cylinders with similar initial height $\hat{H}$ in (c).

The decrease of the slump height with increasing initial radius is a natural consequence of the growth of the rigid core of the dambreak and the eventual emergence of an incomplete slump. Indeed, for the latter, $\mathcal{H}_\infty=1$ and $S=0$, rendering this diagnostic useless for sufficiently large R. Instead, a measure of the degree of slump at the edge of the initial cylinder is provided by the distance fallen by the upper circular corner, which clearly decorates the final deposit except for very low yield stresses (see Figs. 3 and 10). This alternative diagnostic, denoted by $1-\mathcal{H}_c$ where $\mathcal{H}_c$ is the final height of the corner, is compared with S in Figs. 9 and 10. Evidently, $1-\mathcal{H}_c$ is less sensitive to variations in R. Note that, for some of the cylinders with relatively small aspect ratio, our side imaging of the thickness profile obscures the centre of the deposit when the circular corner falls less far; in this situation, the measurement of S is actually given by $1-\mathcal{H}_c$.

Despite the reduced sensitivity of $1-\mathcal{H}_c$ to R, this diagnostic does depend on the rate at which the fluid is released (Fig. 9(b)). Evidently, the speed at which the cylinder is raised affects how much fluid yields at the fluid edge, which partly controls the fall there. Indeed, the release rate correlates closely with the amount of material left on the cylinder after it is raised (which we measured on a weigh scale in this series of experiments; see Fig. 9(b)). The impact of the release mechanism on the degree of slump has been reported previously [5], and includes the possibility that both inertia and adhesion to the cylinder play important roles in the dynamics. Here, our goal is to complement our inertia less axisymmetric dambreak computations with similar, if not identical experiments, and so the effect of the release mechanism is a distraction that precludes a quantitative comparison of theory and experiment. In particular, the action of lifting the cylinder must force the fluid to yield even if $B>B_c$, which may well explain why the existing experimental data at higher B does not progress to the unyielded slump value $S=0$ ($0.265<B_c<1/\sqrt{3}\approx 0.577$ over the full range of R).

Fig. 10 compares in more detail the experimental slump heights with the results of our simulations. The two agree qualitatively, if not quantitatively, with the wider initial cylinders of the simulations slumping less far. The comparison is worse for previously reported numerical data [5,7,13] for Bingham slumps, which mostly collapse even further. We suspect that this is due to resolution issues, as illustrated in Fig. 5.

Fig. 11 shows another comparison of the final central depth and radius of the deposit against yield stress. Here, the data is scaled by $R^{2/3}$, which corresponds to choosing a length scale based on the initial volume of the cylinder rather than its height, and constitutes a more natural choice in the shallow limit where much of the memory of the initial shape is lost. The rescaling collapses both the height and radius data close to a common curve matching the asymptotic prediction from (11) (at least for the aspect ratios used in the plot, with $R<4$), in contrast with the slump height diagnostic of Figs. 9 and 10.

Previous experiments have also invariably been conducted over smooth surfaces. However, it is known [31] that spreading drops of viscoplastic fluid can suffer effective slip unless the surface is either chemically treated or roughened. Indeed, when we conduct slumps over the smooth plexiglass, the fluid collapses noticeably further, implying a degree of slip (the contact angle is also noticeably different, exceeding 90° for the roughened surface, but not for the smooth one). By contrast, slumps over a surface covered with sandpaper are similar to those above our roughened plexiglass, providing confidence that our surface roughening significantly reduces slip in the bulk of our tests. Fig. 12 compares the final shapes of a particular slump conducted over the different three surfaces, and Fig. 9(b) includes data for the same slump over the smooth plexiglass.

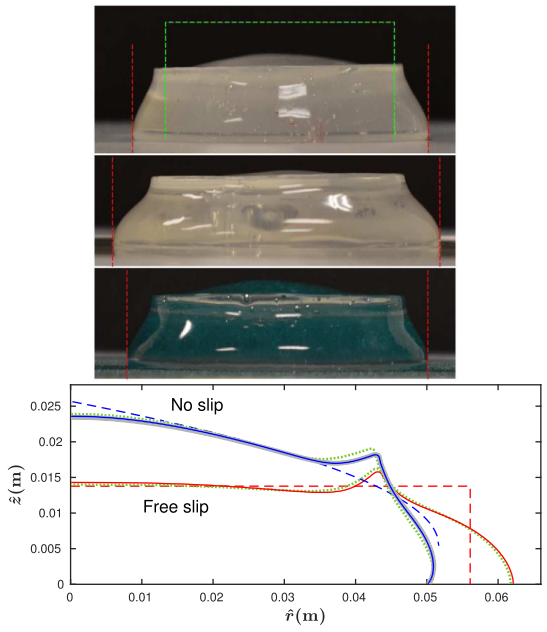

Fig. 12. Side images from the slump experiments and theoretical final profiles: the photographs compare slumps over the roughened, smooth and (green) sandpaper surfaces (from top to bottom); vertical dashed lines indicate the final radii, and the scale of the photographs is indicated in the first panel, for which the rectangle shows the initial fluid cylinder, of height 3 cm and radius 3.8 cm. The plot shows computations matching the experiments ($R = 1.29$, $B = 0.13$ and $\mathrm{Re} = 0.28$) and using the surface boundary conditions indicated (blue line for no slip, red for free slip); the dashed lines indicate the shallow-layer asymptotic predictions in (11) and (C.9). For the no slip case, two other computations are shown: a computation with artificially high Reynolds number ($\mathrm{Re} = 35$; thick grey line) and one with Herschel–Bulkley model ($n = 0.3$; green dots). For the free slip case, the green dots again show a computation with the Herschel–Bulkley model ($n = 0.3$). (For interpretation of the references to color in this figure legend, the reader is referred to the web version of this article.).

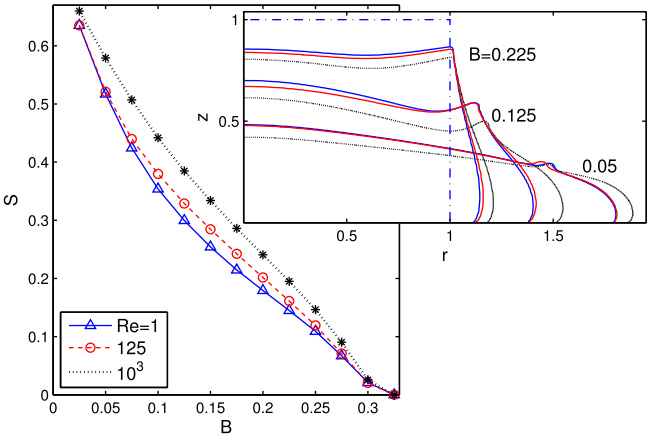

Fig. 13. The dimensionless slump height for cylindrical dambreaks with $R = 1$, varying B and the Reynolds numbers indicated. The inset shows three sample triplets of the final shape at the Bingham numbers indicated.

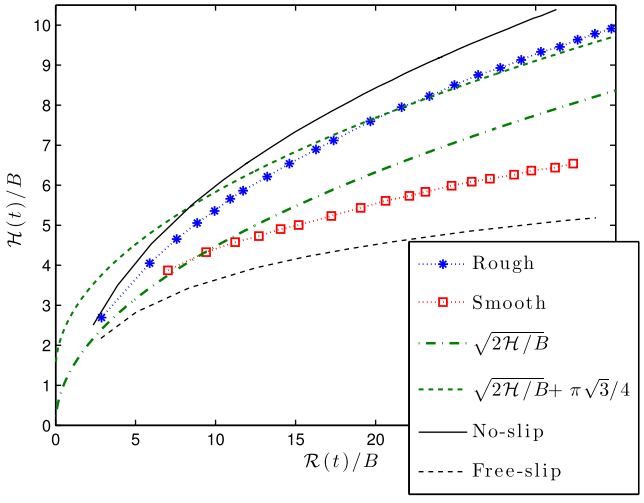

Fig. 14. Maximum radius $\mathcal{R}(t)/B = \rho g \hat{R}/\tau_Y$ *versus* depth $\mathcal{H}(t)/B = \rho g \hat{H}/\tau_Y$ for experimental extrusions with a pump rate of 31.5 ml/min over the rough (stars) and smooth (squares) plexiglass. Also plotted are the leading-order and improved asymptotic predictions, and Herschel–Bulkley simulations matching the physical parameters of the experiment with either no slip or free slip boundary conditions.

For a theoretical examination of the effect of surface slip, we conduct simulations in which the no slip condition is replaced by free slip (*i.e.* we impose $\tau_{rz} = 0$ at $z = 0$). Fig. 12 compares the result with that using no slip for simulations in which the geometrical parameters and yield stress are matched to the experiments. A free slip version of the asymptotic analysis for shallow flows can also be provided, as summarized in Appendix C; the final shape is predicted to remain cylindrical, with a depth of $2B\sqrt{3}$ and a radius of $R/(12B^2)^{1/4}$. Both this prediction and that of the improved no slip theory in (11) are also plotted in Fig. 12. The fluid spreads noticeably further with free slip, mirroring the experiments. The spread over the smooth plexiglass is, however, rather less significant than suggested by the free slip computations, as would be the case if there was a residual surface interaction.

Fig. 12 also includes results from a simulation in which inertial effects are promoted by taking a higher Reynolds number than that matching the experimental conditions (Re is about 125 times higher in this case). The two solutions can barely be distinguished in the figure, highlighting how inertia plays little role in controlling the final shape in the simulations. Indeed, our computations suggest that inertial effects are relatively minor over most of the range of physical conditions of our experiments: Fig. 13, shows the slump height S and sample final profiles for computations with $R = 1$ and varying B and Re. Inertia plays no role in controlling the final shape for $\mathrm{Re} < 1$; the slump height increases for higher Reynolds number, but the effect is modest for our experiments (with $\mathrm{Re} < 125$).

A final feature of Fig. 12 is the inclusion of computations using the Herschel–Bulkley model in (20), rather than the Bingham law (for both no slip and free slip surfaces). Evidently, as alluded to earlier, the power-law viscosity has little effect on the final shape. However, there do appear to be some minor quantitive differences, especially in the vicinity of the corner stemming from the upper edge of the initial cylinder. It is conceivable that these result from differences in the time evolution of the plugs during the collapse, which then impacts the final deposit. Otherwise, the viscous stress is not expected to feature directly in the force balance controlling the final shape. Nevertheless, any differences in the final radius and height that may be introduced in this manner from the power-law rheology are unlikely to upset the comparison of experiments and Bingham theory in Figs. 9–13.

4.3. Extrusions

The impact of the release mechanism on the slump is removed in experiments in which fluid is extruded slowly from a vent onto the underlying surface, allowing a clearer examination of the effect of surface slip and a more quantitative comparison with theory. Results of a sample extrusion are shown in Fig. 14, which plots the instantaneous radius $\mathcal{R}(t)/B = \rho g \hat{R}/\tau_Y$ against central depth $\mathcal{H}(t)/B = \rho g \hat{H}/\tau_Y$, both scaled by B. Rescaling the results in this way removes the scaling by

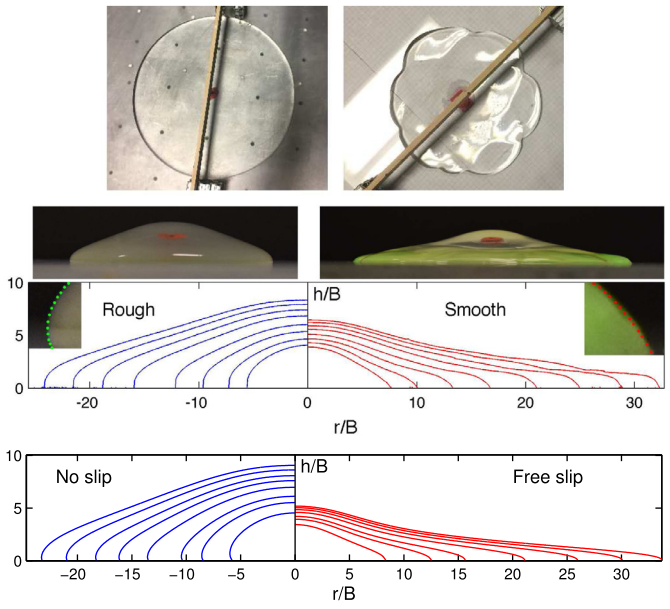

Fig. 15. Images and profiles from the extrusion experiments also shown in Figure 14. The top images show top and side images of an extrusion over the rough (left) and smooth (right) plexiglass (a ruler straddles the extrusions to add a scale for the side images). The first row of plots underneath show a sequence of height profiles at similar times (extruded volumes; the side photographs correspond to the sixth profiles). The insets show magnifications of the contact line. The lowest row of plots shows height profiles from corresponding numerical simulations applying either a no slip (left) or a free slip (right) boundary condition on $z = 0$ (less one profile for the free slip case). The times of the snapshots are not perfectly matched owing to irregularities in pump rate in the experiments.

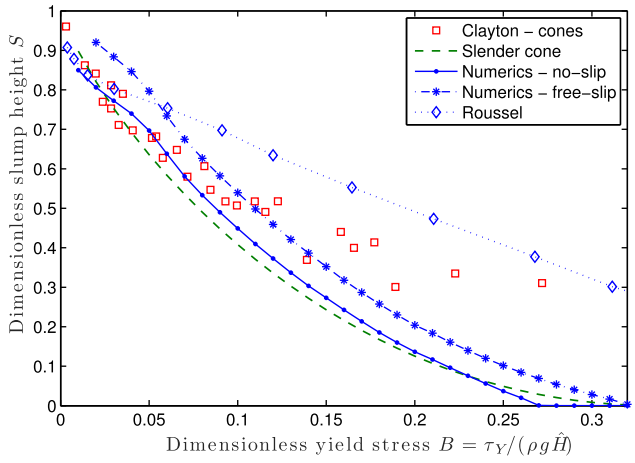

Fig. 16. Slump heights for Bingham dambreaks with an initially conical shape corresponding to the ASTM standard, computed using a no slip (solid line with points) or free slip (dashed-dotted line with stars) condition on the underlying plane. Squares show experimental data from [4]. The dashed line shows the prediction for a slender conical column in Appendix D. The diamonds show the results of numerical computations of [9].

$\hat{H}$ implicit in the non-dimensionalization of the problem in Section 2, which has no meaning for the extrusions. Instead, distance is scaled by the length scale $\tau_Y/\rho g$.

Fig. 14 includes data from an extrusion with similar pump rate over the smooth plexiglass. The radius-height relation, $\mathcal{R}/B$ *versus* $\mathcal{H}/B$, is very different and reflective of a shallower flow. This is illustrated further in Fig. 15, which displays sample images and height profiles taken from the experiments. In fact, the extrusions over the smooth plexiglass became noticeably non-axisymmetric over late times, developing interesting lobe patterns towards the rim of the extruded dome (see the images shown at the top of Fig. 15). It is not clear whether these patterns reflects an intrinsic instability of sliding extensional flow [cf. 32] or a more pronounced sensitivity to surface imperfections at the contact line.

When the extrusion flux is relatively small, the developing dome above the vent is expected to be close to a steady equilibrium state, allowing us to recycle the shallow asymptotics of Section 3.1. In particular, the radius-height relation from (11) is

$$\frac{\mathcal{H}}{B} \sim \sqrt{\frac{2\mathcal{R}}{B}} + \frac{\pi\sqrt{3}}{4}, \tag{21}$$

which is also included in Fig. 14, along with the leading-order result $\mathcal{H}/B = \sqrt{2\mathcal{R}/B}$. The improved model in (21) is unrealistic for $\mathcal{R} \to 0$, where the invalid treatment of the edge predicts a finite central depth, which is the analogue of the vertical cliff predicted at the fluid edge by (11).

For equivalent numerical computations, we perform simulations as outlined in Section 2, but using the Herschel–Bulkley law and replacing the no-penetration condition $w(r, 0, t) = 0$ with $w(r, 0, t) = 2\pi^{-1}(R_v^2 - r^2)/R_v^4$ for $r < R_v$, where R_v is the dimensionless radius of the vent. As initial condition, we take $c(r, z, 0) = 0$ everywhere except over a shallow prewetted film spanning the vent and of depth 0.05. In these computations, $\hat{H}$ no longer has any meaning as the characteristic height of the initial configuration, but can be defined using the net dimensional flux $\hat{Q}$: in view of our prescription for the vertical velocity, the dimensionless flux is unity, so that $\hat{Q} = \hat{H}^2 U = \hat{H}^2(\rho g \hat{H}^{1+n}/K)^{1/n}$. Thus, $\hat{H} = \left(K\hat{Q}^n/\rho g\right)^{1/(1+3n)}$.

A numerical simulation designed to match the experimental conditions is included in Figs. 14 and 15. The numerical simulation over-predicts the central height in comparison to the experiments, but otherwise tracks the observed radius-height relation. The comparison of surface profiles illustrates how the theory reproduces the shape of the observed extruded dome, but again reveals the slight discrepancy between theory and experiment. We suspect that this originates from the incomplete removal of slip over the underlying roughened plexiglass surface (fluid in the experimental extrusion flows further than in the simulation and the side profiles are less steep). However, errors in the fluid rheology (the Herschel–Bulkley fit, or non-ideal properties of the Carbopol) might also be responsible.

Figs. 14 and 15 also include simulations results for a computation in which the no slip condition on $z = 0$, $r > R_v$, is replaced by free slip. As for the axisymmetric dambreaks, the enhanced spread of the fluid and the attendant modification in the height profile are reminiscent of how the experiments on the smooth plexiglass differ from those above the roughened surface, reinforcing our conclusions regarding surface slip. Once more, however, the freely sliding computations spread even further than the extrusions on smooth plexiglass, suggestive of residual surface traction.

5. Concluding remarks

In this paper, we have presented a theoretical analysis of the axisymmetric dambreak of a cylinder of viscoplastic fluid, and compared the results with experiments using a Carbopol gel. In the theory, we used computations with either a regularized Bingham model or an augmented-Lagrangian scheme to study the fluid slump, complemented by asymptotic analyses relevant for shallow gravity currents or tall thin columns. We also examined the states at the brink of failure to determine the conditions under which the initial cylinder does not collapse.

The computations, which are based on the VOF method to track the fluid interface, are complicated significantly by the need to resolve the flow adjacent to the underlying no slip surface. Without special attention to this detail, computations inevitably become unresolved and spread excessively far as a result. Both this and inaccurate treatments of the yield stress likely reduce the reliability of slump test computations. Here,

we adopted a numerical device which ensures that our computations remain resolved, and acts by adjusting the fluid interface and allowing the contact line to move over the surface.

For dambreaks (cylindrical slump tests), theory and experiment agree qualitatively and are consistent with previous experiments that measure the dimensionless "slump height" (the distance fallen by the centre of the cylinder divided by the initial height), and use a variety of different kinds of (less ideal) viscoplastic fluids. However, one must be careful to eliminate slip over the underlying surface, which can significantly enhance the collapse. Moreover, the mechanism by which the fluid is released introduces quantitative differences between theory and experiment, either through the interaction with the lifted container, or *via* the amount of inertia imparted at the moment of release. The effect of the release mechanism is avoided when fluid is pumped slowly through a vent onto the surface. In such extrusions, the agreement between theory and experiment is improved, although there are some remaining differences that are most likely due either to residual slip or an inaccurate treatment of fluid rheology.

A main motivation of the current work was to shed further light on the fluid dynamics of the slump test. That practical device exploits a conical initial shape rather than a cylinder, begging the question of how the present results carry over to this other geometry. Fig. 16 plots simulation results for the slump height computed for Bingham fluid with an initial shape given by an ASTM standard cone (which is 30 cm high, with a top radius of 5 cm and a basal radius of 10 cm). As for the cylinder, the theoretical slumps do not collapse as far as experiments (this time taken from [4]) at higher yield stresses, a discrepancy that could arise from either the release mechanism or slip. However, although the threshold for failure depends on the slip condition on the underlying surface ($B_c \approx 0.27$ or 0.32 for this geometry with either no or free slip, respectively), the continued significant slump of the experimental cones for higher yield stress suggests that the release mechanism, not slip, is more important. Except for low yield stresses, the simulations results also disagree significantly with those reported by Roussel and Coussot [9], especially for the failure criterion.

Acknowledgements

S.H. acknowledges financial support by NSF (Grant No. CBET-1554044-CAREER).

Appendix A. Numerical convergence study

Fig. A.17 shows the results of a resolution study for the runout of a Newtonian slump with $R = 1$ and varying grid size. The first panel presents results for the PLIC scheme with the non-conservative correction of [15]; those with the conservative correction are plotted in the second panel. Both are compared with the results of lubrication theory [12,33]. Also included in Fig. A.17(b)–(c) are corresponding results for the runout of a Bingham slump with $B = 0.05$ and a comparison of the fluid interfaces of the various solutions at $t = 250$, all for the case of the PLIC scheme with the conservative correction (and both values of B).

Fig. A.18 shows further details of the resolution studies with $B = 0$ and 0.05, plotting the runout and central depth of the slump at $t = 250$ for various computations with differing resolution. Computations both with and without the correction schemes are presented; the results for the original PLIC algorithm converge much more slowly than those for the corrected schemes, with the conservative correction scheme being superior. For $B = 0.05$, the three different treatments of the interface are shown for a computation using the regularization method to deal with the yield stress. Also shown is a series of computations using the augmented-Lagrangian method and the PLIC scheme with a conservative correction, which illustrates how the two methods for the dealing with the yield stress yield similar results.

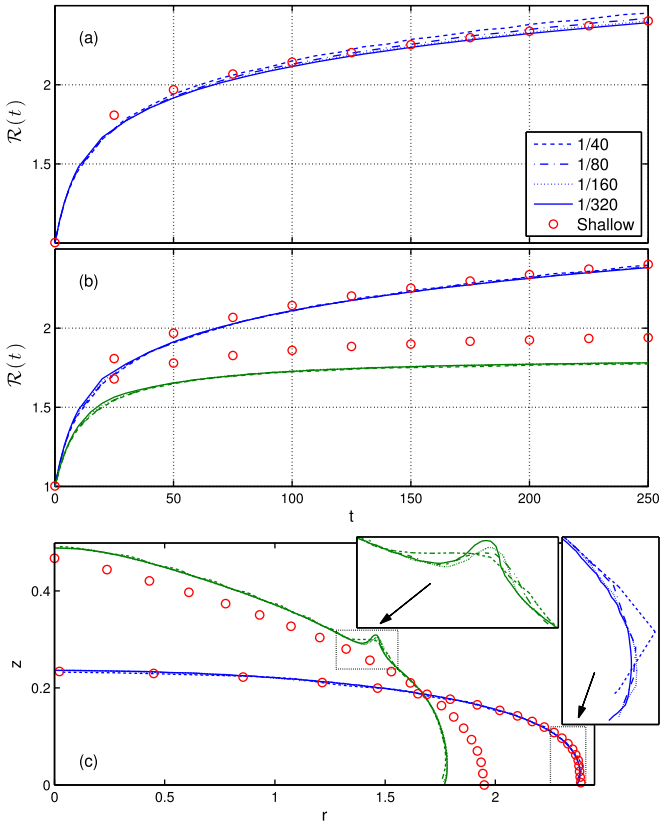

Fig. A17. Computations with varying grid size (as indicated). Panels (a) and (b) show the flow front as a function of time for a Newtonian slump with $R = 1$ using the PLIC scheme with the non-conservative and conservative corrections, respectively. Also inclued in (b) are corresponding results for a Bingham slump with $B = 0.05$ (green curves). Panel (c) shows the interfaces at $t = 250$ of the computations in (b) (with inset showing magnifications near the flow fronts). The red circles show leading-order shallow-layer solutions [33,34] (For interpretation of the references to color in this figure legend, the reader is referred to the web version of this article.).

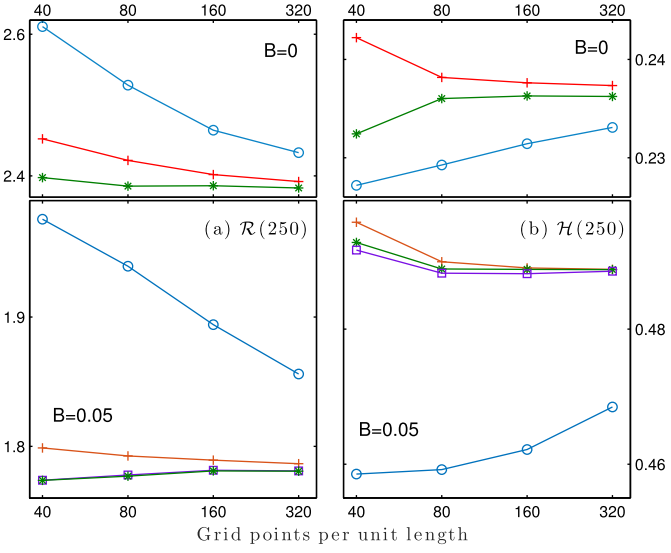

Fig. A18. (a) Runout and (b) central depth at $t = 250$ with varying grid size for a Newtonian ($B = 0$; top) and Bingham slump ($B = 0.05$; bottom) using various interface-tracking schemes and Navier–Stokes solvers: regularization with the PLIC algorithm including the non-conservative (crosses), conservative (stars) or no correction (circles) scheme, or using the augmented-Lagrangian method with PLIC and the conservative correction (squares). There is no difference between the Navier–Stokes solvers for $B = 0$.

Appendix B. Higher-order shallow asymptotics

When flow becomes arrested, throughout the bulk of the fluid the constitutive model reduces to the plasticity law $\tau_{ij} = B\dot{\gamma}_{ij}/\dot{\gamma}$. In combination with the rescaled equations in (7) and (10), one may then deduce the leading-order stress components,

$$\begin{cases} \check{\tau}_{rz} = \check{B}(1 - z/h_0), \\ (\check{\tau}_{rr}, \check{\tau}_{\theta\theta}) = \check{B}(u_\chi, \chi^{-1}u)\dfrac{\sqrt{1-(1-z/h_0)^2}}{\sqrt{u_\chi^2 + u^2/\chi^2 + uu_\chi/\chi}}, \end{cases} \tag{B.1}$$

where $h_0 = \sqrt{1 - \chi/\chi_\infty}$ and u are the leading-order profile and radial velocity, with $\chi_\infty \equiv \epsilon r_\infty$. If we instead neglect only the $O(\epsilon^2)$ terms in (7) and (8), we find that $p + \epsilon\check{\tau}_{zz} = h - z + O(\epsilon^2)$. An integral of the radial force balance over the depth of the fluid then furnishes the equation

$$hh_\chi + \check{B} = \frac{3\epsilon}{2}\frac{d}{d\chi}\left[\int_0^{h_0}(\check{\tau}_{rr} + \check{\tau}_{\theta\theta})dz\right] + \frac{\epsilon}{2\chi^2}\frac{d}{d\chi}\left[\chi^2\int_0^{h_0}(\check{\tau}_{rr} - \check{\tau}_{\theta\theta})dz\right]. \tag{B.2}$$

To correct the profile, we evaluate the $O(\epsilon)$ terms on the right of (B.2) using the leading-order stress components.

In order to accomplish this, however, we must first determine the leading-order radial velocity u in order to fix the indeterminacy of the axisymmetric stress components. The convergence of the leading-order slump solution to rest has been explored previously in [12], extending the work of Matson and Hogg [35] for 2D dambreaks. It was found that, for $t \to \infty$, the radial velocity u is plug-like throughout the fluid depth and given by $u = Q_\xi^2/(4\xi)$, where

$$\frac{d}{d\xi}\left[(1-\xi^2)Q_\xi^2\right] = 2\lambda(1-\xi^2)(1-Q), \tag{B.3}$$

with $\xi = \sqrt{1 - \chi/\chi_\infty}$ and $\lambda \approx 23.3855$. With the solution of this problem in hand, we may then compute $\check{\tau}_{rr}$ and $\check{\tau}_{\theta\theta}$ to leading order. The results are compared with components extracted from the numerical simulations in Fig. B.19(a) for a sample slump near the arrest of motion. Plotted are the stress components along the level where $\tau_{rz} = 0$ (which is $z = h_0$ in the leading-order asymptotics), after recasting the asymptotic predictions in terms of the original variables. Except near the centre and edge of the collapsed cylinder (where the shallow-layer asymptotics breaks down), the two agree qualitatively. Evidently, τ_{zz} is almost constant in radius, whereas τ_{rr} and $\tau_{\theta\theta}$ match one another up to a small correction.

The approximation $\check{\tau}_{rr} \approx \check{\tau}_{\theta\theta}$ (which corresponds to a plug speed $u \propto r$; *cf.* Fig. B.19(b)), offers a simpler analytical pathway to a corrected final profile: the yield condition now implies that

$$\check{\tau}_{rr} + \check{\tau}_{\theta\theta} \approx \frac{2\check{B}}{\sqrt{3}}\sqrt{1 - \left(1 - \frac{z}{h_0}\right)^2}, \tag{B.4}$$

and so the corrected profile now follows from (B.2) as

$$hh_\chi + \check{B} \sim \frac{\pi\sqrt{3}}{4}\epsilon\check{B}h_\chi, \tag{B.5}$$

which provides the solution quoted in Section 3.1.

Appendix C. Shallow slippy flows

When the fluid slides more freely over the underlying surface, the lubrication model of [23] no longer captures the leading-order dynamics. In particular, the extensional stress components (τ_{rr}, $\tau_{\theta\theta}$, τ_{zz}) become promoted to higher order in comparison to the shear stress τ_{rz} because the reduced surface traction generates little vertical shear and the horizontal flow becomes plug-like throughout the fluid layer. In this circumstance, the relevant asymptotic description is that of a viscoplastic membrane model [36]: rather than rescaling as in Section 3.1, we set only $\tau_{rz} = \epsilon\check{\tau}_{rz}$. Then, ignoring inertia, the leading-order momentum equations are

$$0 = -p_\chi + \frac{1}{\chi}(\chi\tau_{rr})_\chi + \check{\tau}_{rz,z} - \frac{\tau_{\theta\theta}}{\chi} + O(\epsilon), \tag{C.1}$$

$$0 = -p_z + \tau_{zz,z} - 1 + O(\epsilon), \tag{C.2}$$

With the rescaled horizontal velocity $u \sim \epsilon^{-1}\check{u}(\chi, t) \gg w(\chi, z, t)$, the constitutive law predicts that

$$(\tau_{rr}, \tau_{\theta\theta}) \sim 2\left(1 + \frac{B}{\dot{\gamma}}\right)(\check{u}_\chi, \check{u}/\chi), \tag{C.3}$$

$$\dot{\gamma} \sim 2\sqrt{\check{u}_\chi^2 + \check{u}\check{u}_\chi/\chi + \check{u}^2/\chi^2}, \tag{C.4}$$

which are independent of z. The surface boundary conditions in (8) are replaced by

$$\left.\begin{matrix}\check{\tau}_{rz} + h_\chi(\tau_{rr} - p) \\ p + \tau_{zz}\end{matrix}\right\} = O(\epsilon) \text{ on } z = h. \tag{C.5}$$

The integral of (C.2) now furnishes $p + \tau_{zz} = h - z$ to leading order. From the depth integrated continuity equation and (C.1), it then follows that

$$h_t + \frac{1}{\chi}(\chi h\check{u})_\chi = 0, \tag{C.6}$$

$$0 = -h_\chi - \frac{\tau_b}{h} + \frac{1}{h}\left[h(2\tau_{rr} + \tau_{\theta\theta})\right]_\chi + \frac{\tau_{rr} - \tau_{\theta\theta}}{\chi}. \tag{C.7}$$

Here $\tau_b = \check{\tau}_{rz}(r, 0, t)$ is the basal shear stress, which must be specified by an additional model of slip.

For a cylindrical dambreak with free slip ($\tau_b = 0$), the equations admit a simple solution in which the fluid retains the shape of a cylinder, with $h = \mathcal{H}(t)$ and $\check{u} = \chi\mathcal{U}(t)$ for $\chi < \epsilon\mathcal{R}(t)$, and $\dot{\mathcal{R}} \equiv \mathcal{R}\mathcal{U}$. The extensional stresses become $\tau_{rr} = \tau_{\theta\theta} = 2\mathcal{U} + B/\sqrt{3}$, and mass conservation demands that $\mathcal{R}^2\mathcal{H} = R^2$. Although (C.7) is now satisfied, the combined gravitational and extensional stress must still vanish at the edge of the cylinder, which implies that $-\frac{1}{2}\mathcal{H}^2 + \mathcal{H}(2\tau_{rr} + \tau_{\theta\theta}) = 0$, or $\frac{1}{2}\mathcal{H} = 6\mathcal{U} + B\sqrt{3}$. Thus,

$$\dot{\mathcal{H}} = -2\mathcal{H}\frac{\dot{\mathcal{R}}}{\mathcal{R}} = \tfrac{1}{6}R\sqrt{\mathcal{H}}(B\sqrt{3} - \tfrac{1}{2}\mathcal{H}). \tag{C.8}$$

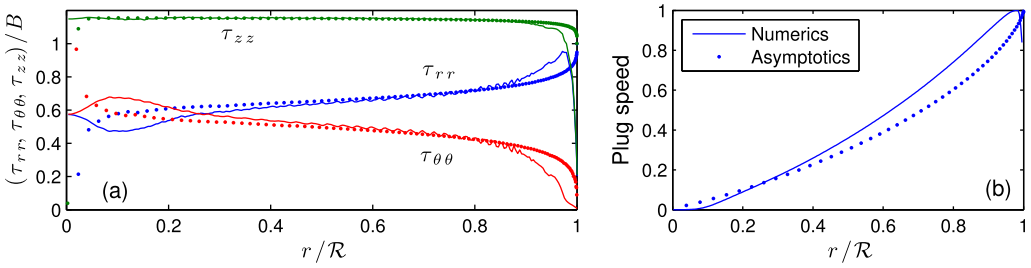

Fig. B19. (a) Scaled stress components (τ_{rr}, $\tau_{\theta\theta}$, τ_{zz})/B and (b) radial speed $u/u_{\max}$ plotted against $r/\mathcal{R}$ along the level where $\tau_{rz} = 0$ at the end of the computation of a simulation with $B = 0.01$ and $R = 1$.

Provided $B < 1/(2\sqrt{3})$, the cylinder therefore collapses to a final state given by

$$\mathcal{H} = 2B\sqrt{3} \qquad \text{and} \qquad \mathcal{R} = \frac{R}{(12B^2)^{1/4}}. \tag{C.9}$$

Appendix D. Tall slender cones

Most practical slump tests take a truncated cone as the initial shape with the radius at the top equal half of that at the base. The slender analysis in this case has been derived by Clayton et al. [4] using the Tresca yield condition. For von Mises, the corresponding result is

$$s = 1 - h_0 - \sqrt{3}B \ln\left(\frac{\left(1+\alpha^{-1}\right)^3 - 1}{\left(1+\alpha^{-1}h_0\right)^3 - 1}\right), \tag{D.1}$$

where h_0 is the height of the unyielded region, given by

$$B = \frac{\alpha}{3\sqrt{3}} \frac{\left(1+\alpha^{-1}h_0\right)^3 - 1}{\left(1+\alpha^{-1}h_0\right)^2}$$

and $\alpha = R_{\text{top}}/(R_{\text{base}} - R_{\text{top}})$.

Supplementary material

Supplementary material associated with this article can be found, in the online version, at doi:10.1016/j.jnnfm.2018.04.012.

References

[1] N.J. Balmforth, I. Frigaard, G. Ovarlez, Yielding to stress: recent developments in viscoplastic fluid mechanics, Ann. Rev. Fluid Mech. 46 (2014) 121–146.
[2] N. Pashias, D.V. Boger, J. Summers, D.J. Glenister, A fifty cent rheometer for yield stress measurement, J. Rheol. (N.Y.) 40 (1996) 1179.
[3] A.W. Saak, H.M. Jennings, S.P. Shah, A generalized approach for the determination of yield stress by slump and slump flow, Cem. Concr. Res. 34 (2004) 363–371.
[4] S. Clayton, T.G. Grice, D.V. Boger, Analysis of the slump test for on-site yield stress measurement of mineral suspensions, Int. J. Miner. Process. 70 (2003) 3–21.
[5] J. Gao, A. Fourie, Spread is better: an investigation of the mini-slump test, Miner. Eng. 71 (2014) 120–132.
[6] C. Famiglietti, J. Prevost, Solution of the slump test using a finite deformation elasto-plastic Drucker–Prager model, Int. J. Numer. Methods Eng. 37 (22) (1994) 3869–3903.
[7] M.R. Davidson, N.H. Khan, Y.L. Yeow, Collapse of a cylinder of Bingham fluid, ANZIAM J. 42 (2000) 499–517.
[8] J.E. Sader, M.R. Davidson, Scaling behavior for gravity induced flow of a yield stress material, J. Rheol. (N.Y.) 49 (1) (2005) 105–112.
[9] N. Roussel, P. Coussot, Fifty-cent rheometer for yield stress measurements: from slump to spreading flow, J. Rheol. (N.Y.) 49 (2005) 705.
[10] A. Bouvet, E. Ghorbel, R. Bennacer, The mini-conical slump flow test: analysis and numerical study, Cem. Concr. Res. 40 (2010) 1517–1523.
[11] N. Roussel, A. Gram, M. Cremonesi, L. Ferrara, K. Krenzer, V. Mechtcherine, S. Shyshko, J. Skocec, J. Spangenberg, O. Svec, L.N. Thrane, K. Vasilic, Numerical simulations of concrete flow: a benchmark comparison, Cem. Concr. Res. 79 (2016) 265–271.
[12] N.J. Balmforth, R.V. Craster, A.C. Rust, R. Sassi, Viscoplastic flow over an inclined surface, J.Non-Newtonian Fluid Mech. 142 (2007) 219–243.
[13] J.-M. Piau, Axisymmetric slump and spreading of cohesive plastic soft materials: a yield stress measurement by consisto-rheometry, J. Rheol. (N.Y.) 49 (6) (2005) 1253–1276.
[14] J.A. Chamberlain, D.J. Horrobin, K.A. Landman, J.E. Sader, Upper and lower bounds for incipient failure in a body under gravitational loading, J. Appl. Mech. 71 (2004) 586–589.
[15] Y. Liu, N.J. Balmforth, S. Hormozi, D.R. Hewitt, Two dimensional viscoplastic dambreaks, J. Non-Newton Fluid Mech. 238 (2016) 65–79.
[16] M. Fortin, R. Glowinski, Augmented Lagrangian Methods: Applications to the Numerical Solution of Boundary-Value Problems, North-Holland, 2006.
[17] A. Wachs, Numerical simulation of steady Bingham flow through an eccentric annular cross-section by distributed lagrange multiplier/fictitious domain and augmented lagrangian methods, J. Non-Newton Fluid Mech. 142 (2007) 183–198.
[18] S. Hormozi, K. Wielage-Burchard, I. Frigaard, Entry and start up effects in visco-plastically lubricated viscous shear flow in pipe, J. Fluid Mech. 673 (2011) 432–467.
[19] D. Gueyffier, J. Li, A. Nadim, R. Scardovelli, S. Zaleski, Volume-of-fluid interface tracking with smoothed surface stress methods for three-dimensional flows, J. Comput. Phys. 152 (1999) 423–456.
[20] M. Renardy, Y. Renardy, J. Li, Numerical simulation of moving contact line problems using a volume-of-fluid method, J. Comput. Phys. 171 (2001) 243–263.
[21] S. Afkhami, S. Zaleski, M. Bussmann, A mesh-dependent model for applying dynamic contact angles to VOF simulations, J Comput Phys 228 (2009) 5370–5389.
[22] I.A. Frigaard, C. Nouar, On the usage of viscosity regularisation methods for visco–plastic fluid flow computation, J. Non-Newtonian Fluid Mech. 127 (2005) 1–26.
[23] K.F. Liu, C.C. Mei, Slow spreading of a sheet of Bingham fluid on an inclined plane, J. Fluid Mech. 207 (1989) 505–529.
[24] R. Hill, The Mathematical Theory of Plasticity, 11, Oxford university press, 1998.
[25] A.V. Lyamin, S.W. Sloan, Lower bound limit analysis using non-linear programming, Int. J. Numer. Methods Eng. 55 (2002) 573–611.
[26] A.V. Lyamin, S.W. Sloan, Upper bound limit analysis using linear finite elements and non-linear programming, Int. J. Numer. Anal. Methods Geomech. 26 (2002) 181–216.
[27] J. Chamberlain, S. Clayton, K. Landman, J. Sader, Experimental validation of incipient failure of yield stress materials under gravitational loading, J. Rheol. (N.Y.) 47 (6) (2003) 1317–1329.
[28] W. Prager, P.G. Hodge, Theory of Perfectly Plastic Solids, Dover, 1968.
[29] J. Chamberlain, J. Sader, K. Landman, D. Horrobin, L. White, Incipient failure of a circular cylinder under gravity, Int. J. Mech. Sci. 44 (2002) 1779–1800.
[30] N.J. Balmforth, I.J. Hewitt, Viscoplastic sheets and threads, J. Non-newton Fluid Mech. 193 (2013) 28–42.
[31] M. Jalaal, N.J. Balmforth, B. Stoeber, Slip of spreading viscoplastic droplets, Langmuir 31 (44) (2015) 12071–12075.
[32] R. Sayag, S.S. Pegler, M.G. Worster, Floating extensional flows, Phys. Fluids 24 (9) (2012) 091111.
[33] H.E. Huppert, The propagation of two-dimensional and axisymmetric viscous gravity currents over a rigid horizontal surface, J. Fluid Mech. 121 (1982) 43–58.
[34] N.J. Balmforth, A.S. Burbidge, R.V. Craster, J. Salzig, A. Shen, Visco-plastic models of isothermal lava domes, J. Fluid Mech. 403 (2000) 37–65.
[35] G.P. Matson, A.J. Hogg, Two-dimensional dam break flows of Herschel–Bulkley fluids: the approach to the arrested state, J. Non-Newtonian Fluid Mech. 142 (2007) 79–94.
[36] N. Balmforth, Viscoplastic asymptotics and other techniques, Viscoplastic Fluids: From Theory to Application, CISM, Springer, 2018.